nature physics

LETTERS

https://doi.org/10.1038/s41567-018-0115-y

On-demand quantum state transfer and entanglement between remote microwave cavity memories

Christopher J. Axline[1,3*], Luke D. Burkhart[1,3*], Wolfgang Pfaff[1,2,3*], Mengzhen Zhang[1], Kevin Chou[1], Philippe Campagne-Ibarcq[1], Philip Reinhold[1], Luigi Frunzio[1], S. M. Girvin[1], Liang Jiang[1], M. H. Devoret[1] and R. J. Schoelkopf[1*]

Coupling isolated quantum systems through propagating photons is a central theme in quantum science[1,2], with the potential for groundbreaking applications such as distributed, fault-tolerant quantum computing[3–5]. To date, photons have been used widely to realize high-fidelity remote entanglement[6–12] and state transfer[13–15] by compensating for inefficiency with conditioning, a fundamentally probabilistic strategy that places limits on the rate of communication. In contrast, here we experimentally realize a long-standing proposal for deterministic, direct quantum state transfer[16]. Using efficient, parametrically controlled emission and absorption of microwave photons, we show on-demand, high-fidelity state transfer and entanglement between two isolated superconducting cavity quantum memories. The transfer rate is faster than the rate of photon loss in either memory, an essential requirement for complex networks. By transferring states in a multiphoton encoding, we further show that the use of cavity memories and state-independent transfer creates the striking opportunity to deterministically mitigate transmission loss with quantum error correction. Our results establish a compelling approach for deterministic quantum communication across networks, and will enable modular scaling of superconducting quantum circuits.

Direct quantum state transfer is a rapid and deterministic scheme for quantum communication with propagating photons in a quantum network[16]. In this protocol, a sending node emits a quantum state as a shaped photonic wavepacket that is then absorbed by a receiving node. This requires strong, tunable coupling between light and matter, as well as efficient transfer of photons at a shared communication frequency; so far, state transfer in optical networks has been highly probabilistic due to inefficiencies in photon coupling and transfer[8]. In contrast, superconducting microwave circuits can combine low loss with strong coupling. This platform is well suited to realize on-demand state transfer, and thus to scale quantum devices in a modular fashion. To this end, superconducting microwave memories and propagating modes have successfully been interfaced to realize controlled photon emission[17–20] and absorption[21–23] independently. Due to the difficulty posed by the need for efficient, frequency-matched photon transfer, however, the goal of deterministic quantum communication at a distance has so far remained elusive.

We implement the deterministic state transfer protocol in ref. [16], employing high-Q superconducting microwave cavities[24] to serve as remote quantum memory endpoints in a simple network (Fig. 1a). Each module can be understood to contain two orthogonal cavity modes (memory and communication) that are coupled by an artificial atom (Fig. 1b). The communication modes—implemented as on-chip stripline resonators—are strongly coupled to either end of a transmission line. Realizing on-demand state transfer requires tunable conversion between memory and communication modes within each module, such that the sender emits the state contained in the memory into the transmission line as a wavepacket with a specified temporal profile, and the receiver absorbs this wavepacket. Amplitude- and phase-controlled coupling are realized using a highly efficient radiofrequency-controlled parametric pumping process, via a single transmon dispersively coupled to both modes (Fig. 1c,d)[20]. In particular, we compute the shape of the pumps used in this process so as to best match the temporal profile of the travelling wavepacket (Supplementary Information). System parameters enable the effective coupling strengths between memories and the transmission line, $\kappa^{s,r}(t)/2\pi$, to be tuned dynamically up to 400 kHz—much larger than the intrinsic single-photon decay rates of the memories, $\kappa_0^{s,r}/2\pi < 0.4$ kHz (Supplementary Information).

Following the original proposal, we insert a circulator into the transmission channel, which enforces the directionality of emission from the sender. The circulator also directs signals reflected off the receiver into an output port, which allows readout of both systems using a single parametric amplifier and heterodyne detection chain. While the memory resonance frequencies need not match, efficient transfer requires that the communication modes be close to resonant compared to their bandwidths ($\kappa_{out}^{s,r}/2\pi \sim 1$ MHz). To compensate for a small offset in resonance frequency due to variation in sample assembly, we equip the receiver with an in situ mechanical frequency tuning mechanism (Supplementary Information).

We begin by characterizing the process by which photons in the sender are emitted, transferred and absorbed into the receiver memory. First, we quantify the efficiency of absorption alone by preparing a small coherent state in the sender memory, and then executing the protocol under one of two conditions (Fig. 2a). In one case, we omit the capture pulses and monitor reflection from the receiver. Here, the emitted wavepacket is fully reflected and recorded by our heterodyne detector (Fig. 2b). In contrast, if we

[1]Departments of Applied Physics and Physics, Yale University, New Haven, CT, USA. [2]Present address: Microsoft Station Q Delft, Delft, the Netherlands. [3]These authors contributed equally: Christopher J. Axline, Luke D. Burkhart and Wolfgang Pfaff.*e-mail: christopher.axline@yale.edu; luke.burkhart@yale.edu; wolfgang.pfaff@microsoft.com; robert.schoelkopf@yale.edu

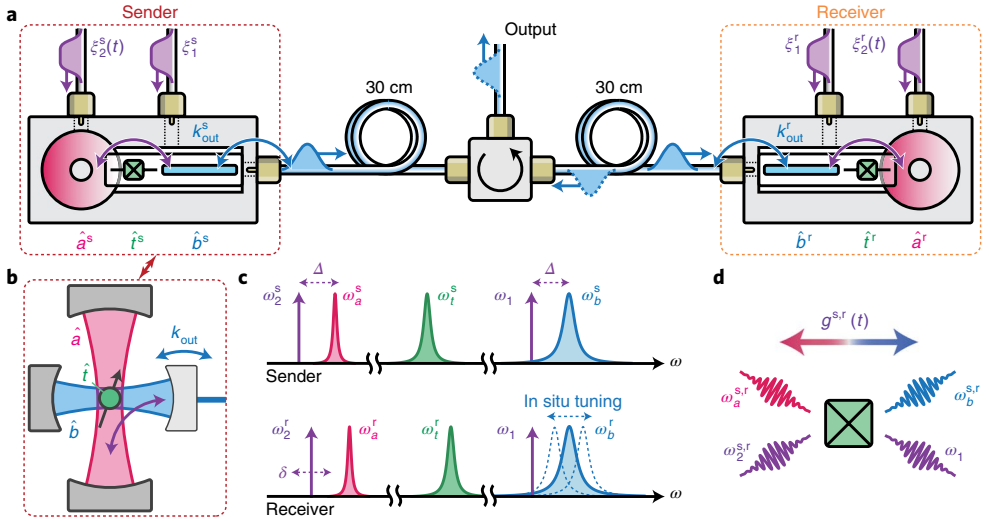

Fig. 1 | On-demand state transfer by parametric conversion. a, Identically constructed circuit quantum electrodynamics sender and receiver modules are connected with a transmission line and a circulator, allowing straightforward measurement of both systems. Each module contains a high-*Q* memory cavity ($\hat{a}$), a transmon qubit ($\hat{t}$) and a communication mode ($\hat{b}$) with strong output coupling κ_{out}. Parametric drives (purple waveforms, ξ) enable conversion between memory and communication modes. **b**, This is equivalent in principle to the memory (red) and communication (blue) modes constituting orthogonal resonant modes whose interaction is mediated by driving an atom (in this case, an artificial atom, the transmon, green). **c**, Frequency ordering of the modes ($\omega_{a,b,t}$) and pumps ($\omega_{1,2}$) in each module. Pumps are applied with a detuning Δ from each mode and an additional relative detuning δ between them to account for Stark shifts. **d**, The parametric conversion process, enabled by the transmon nonlinearity, schematically runs left-to-right in the sender, and right-to-left in the receiver.

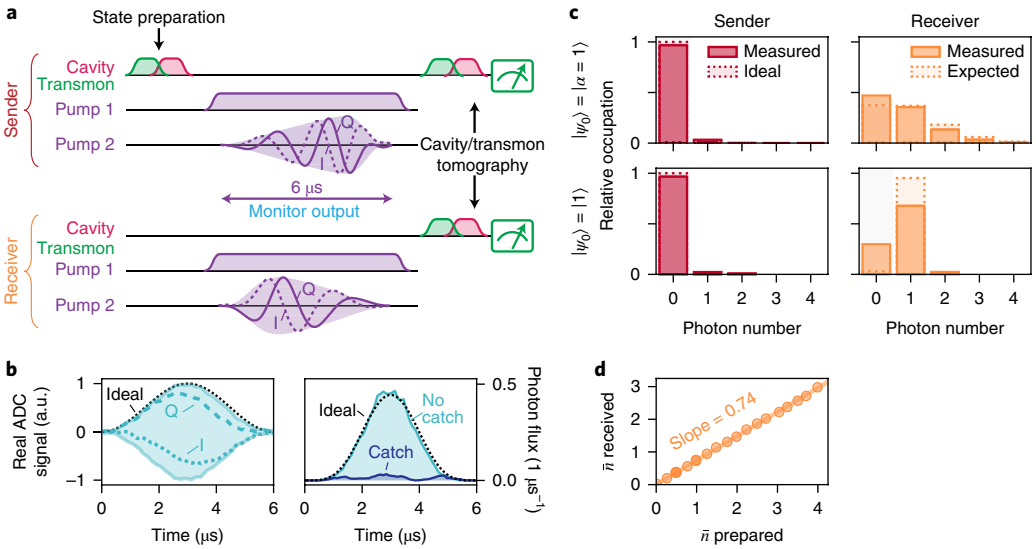

Fig. 2 | Temporal mode-matching of the sender and the receiver. a, The transfer protocol consists of state preparation, pumping and measurement. The sender and the receiver are pumped simultaneously because the propagating wavepacket's time-of-flight (<3 ns) is negligible compared to its width (6 μs). The in-phase (I) and quadrature (Q) components as well as the absolute value (shaded) of the pump modulation tones are shown. **b**, Left: measured field-emission components (I, Q) and envelope (shaded) on release of an $\alpha=1$ coherent state from the sender. Right: photon flux with receiver pumps omitted ('No catch') or applied ('Catch'), demonstrating absorption of the wavepacket. Detector photon flux calibration is inferred by measuring cavity population after release of a one-photon state. The 'Ideal' lines mark the shape and amplitude expected for a complete, uncaught release. **c**, Photon number state occupations of the sender (left) and receiver (right) memory cavities after transfer of an $\bar{n}=1$ coherent state (upper) or $n=1$ Fock state (lower). 'Expected' occupations in the receiver are those measured in the sender after substituting the transfer process with a delay of the same length. **d**, States with $\bar{n}>1$ are transferred with efficiency near those of single-photon states. The line corresponds with the efficiency $\eta=0.74$ measured for single-photon states.

apply the complete set of pulses, this reflection is strongly suppressed. By measuring the relative photon flux at the detector, we determine that the receiver absorbs (93 ± 1)% of the energy contained in the incident wavepacket.

To measure the overall transfer efficiency, we prepare few-photon states and apply both release and capture pulses. We measure cavity populations before and after the transfer using photon number-dependent spectroscopy on the transmon, which directly

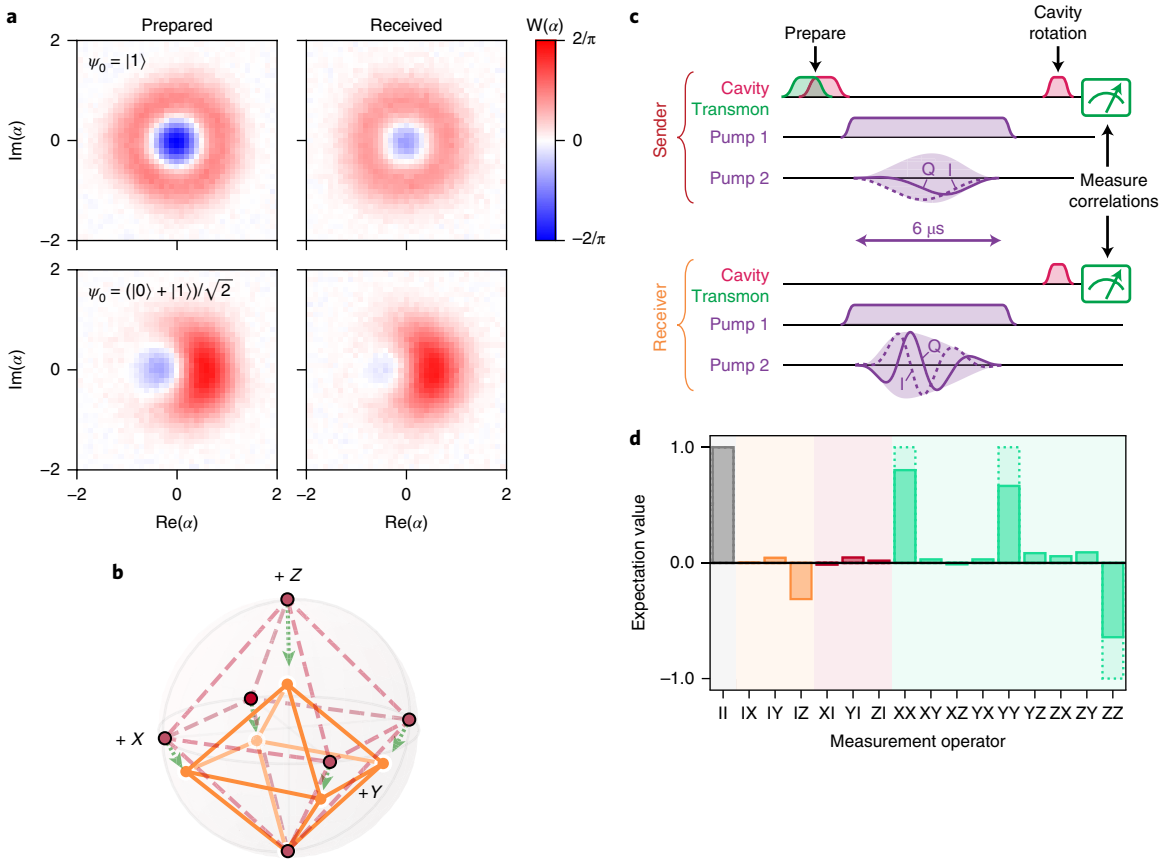

Fig. 3 | Establishing a quantum communication channel. a, Measured Wigner functions of two states encoded in the single-photon manifold $\{|0\rangle, |1\rangle\}$ as prepared in the sender (left) and received following the transfer protocol (right). **b**, The manifold's six cardinal states are visualized in the Bloch sphere as prepared (red, dashed) and received (orange, solid). The green line indicates the position of each prepared state subject to a model of pure photon loss (the tip of the arrowhead denotes an efficiency of 0.74). The octahedron shrinks towards the $|0\rangle$ state as predicted by the loss model. **c**, Single-photon entanglement is generated with a half-release of $|1\rangle$, followed by unchanged capture pulses (shown in the same style as Fig. 2a). Cavity photon number correlations are measured following rotations into the appropriate measurement basis. **d**, Reconstructed expectation values (shaded) of two-qubit Pauli operators compared to those of the maximally entangled Bell state $|01\rangle + |10\rangle$ (dashed). The 'II' operator takes the value of unity here, signifying that the data are conditioned on both transmons remaining in the ground state (Supplementary Information).

provides the relative populations of the cavity number states[25]. We define the transfer efficiency η as the average photon number received divided by the average photon number prepared in the sender. Figure 2c presents the populations of both memories after transferring states with mean photon number $\overline{n} = 1$, from which we calculate an efficiency $\eta = 0.74 \pm 0.03$. Our experimental scheme is independent of input state, verified by measuring the transfer efficiency of a selection of Fock and coherent states with up to $\overline{n} = 4$ (Fig. 2d).

While this transfer efficiency is high, understanding the origin of process imperfections is critical to select optimal error correction protocols and to correct imperfections in future experiments. We can identify several factors that contribute significantly to transfer inefficiency: undesired transmon excitation, imperfectly shaped pump pulses and loss in the transmission path.

For ideal operation of our protocol, the transmons would remain in their ground states during the transfer. However, we observe non-negligible stochastic excitation during the transfer process due to thermalization and pump-induced transitions to higher levels[26,27]. Unwanted transmon excitation has two important consequences. First, an excitation leads to a shift of the resonator frequencies due to their dispersive couplings to the transmon. This abruptly changes the transfer frequency-matching conditions, manifesting as off-resonant emission by the sender, or imperfect wavepacket absorption by the receiver. We estimate these effects to lead to an inefficiency of about 2% for emission, and 6% for absorption (Supplementary Information). This effect is thus likely to be the dominant cause of the measured absorption inefficiency.

Second, transmon excitation precludes effective measurement of the cavity state. In this case, cavity measurement indiscriminately returns 'yes' to a query of any photon number. Excitations thus have the effect of reducing average measurement contrast. By normalizing our measurement data to correct for this, cavity tomography is implicitly conditioned on the transmon having remained in its ground state. It is therefore useful to view the transmon excitation probability as a 'failure probability' of the protocol; that is, we make the conservative assumption that each excitation masks an unsuccessful transfer. The efficiency η quoted above is then conditioned on the receiver transmon remaining in the ground state, with success probability $p_s = 0.87 \pm 0.03$. The conditioned value can be interpreted as the efficiency that would be measured with a perfectly cold transmon or by heralding on a transmon measurement after the protocol (Supplementary Information). The 'deterministic efficiency' given the transmon temperature observed here is estimated by the product of the conditioned efficiency and the success probability, $\eta_d \geq p_s \times \eta = 0.87 \times 0.74 = 0.64 \pm 0.03$. In the transfer characterization to follow, we present both the directly measured (implicitly conditioned) quantities and the estimated deterministic ones. This deterministic value represents a lower bound on the quantity; since these failure events are assumed to be maximally destructive, this is the worst-case scenario (Supplementary Information).

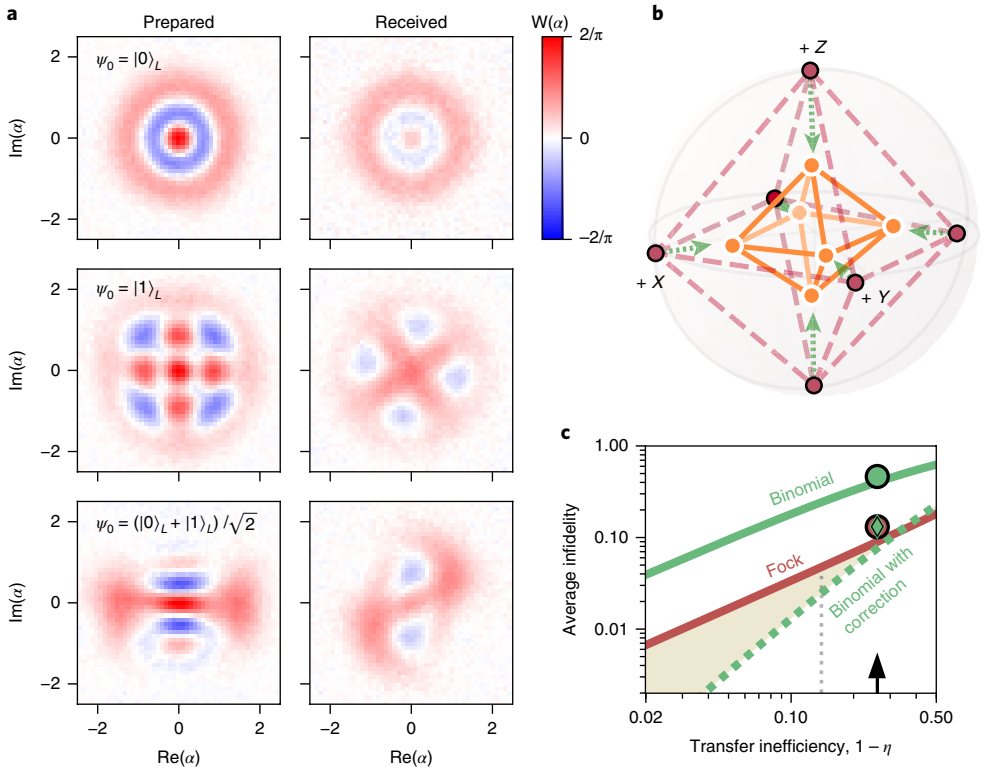

Fig. 4 | Transferring error-correctable states. a, Measured Wigner functions of prepared (left) and received (right) states in the binomial code. Kerr evolution during the transfer results in a distortion in the received state Wigner functions, an effect that is accounted for in fidelity calculation (Supplementary Information). **b**, Bloch sphere representations of prepared (dashed) and received (solid) cardinal states within the binomial encoding. The green dotted arrows indicate the expected shrinkage given the measured efficiency. The octahedron shrinks primarily towards the centre of the sphere as predicted by the loss model for small inefficiency. **c**, Projected performance of the two demonstrated encodings as a function of transfer efficiency. Calculated average infidelity (lines) of Fock and binomial encodings, and measured values (circles) at the present inefficiency (arrow). The performance of an ideal parity detection-and-correction scheme is simulated for the binomial encoding. The resulting infidelities are shown for perfectly prepared states subjected to varying transfer inefficiency (line), and for the measured received states (diamond) (Supplementary Information). Points lie above their respective lines due to small additional infidelity not described by photon loss. The shaded region indicates the regime beyond the break-even point, displaying the growing improvement between the encodings as efficiency improves. Elimination of either transmission loss or release and capture inefficiency would push the corrected infidelity further into this regime ($\eta \sim 0.86$, dotted line).

Additional contributions to transfer inefficiency come from photon loss in the transmission path, which we estimate adds 15%, as well as imperfect pulse shapes affecting state release and capture, each with an effect around 2% (Supplementary Information). We note that the bulk of the described imperfections are not fundamental; in particular, improvements to the transmon equilibrium temperature and thermalization rate as well as parameter engineering to avoid pump-induced higher order transitions[27] can substantially reduce the inefficiencies resulting from transmon excitation.

The achieved transfer efficiency allows for quantum communication between the sender and the receiver memories. We confirm this explicitly by transferring an overcomplete set of qubit states in the manifold spanned by the Fock states $|0\rangle$ and $|1\rangle$, and performing Wigner tomography on the receiver (Fig. 3a). Comparing each received state to the ideal state, we determine an average fidelity $\mathcal{F}_{\mathrm{avg}} = 0.87 \pm 0.04$ (deterministic: $\mathcal{F}_{\mathrm{avg,d}} \geq p_{\mathrm{s}} \times \mathcal{F}_{\mathrm{avg}} = 0.76 \pm 0.04$). Both the conditioned and deterministic fidelities significantly exceed the classical bound of 2/3, the maximum attainable fidelity with which one can reconstruct an unknown qubit state using only classical communication[28].

Importantly, the measured fidelity $\mathcal{F}_{\mathrm{avg}}$ is consistent with that expected (0.91 ± 0.03) from a pure photon loss model using the measured transfer efficiency. A representation of prepared and received states as vertices of an octahedron on the Bloch sphere (Fig. 3b) reveals a systematic shrinkage towards $|0\rangle$ that also appears consistent with photon loss. More quantitatively, we find that the measured transfer has a process fidelity of 0.95 to this single-source model, bounding the errors not described by photon loss at the 5% level (Supplementary Information).

Our experimental scheme readily enables us to generate on-demand remote entanglement by applying a pump sequence on the sender that releases half of its stored energy (Fig. 3c). If the initial state is a single photon, this results in entanglement between the memory and the emitted radiation[20]. Subsequent absorption of the wavepacket by the receiver ideally results in the Bell state $(|10\rangle + |01\rangle) / \sqrt{2}$ shared between the memories. We perform joint tomography following this protocol, revealing non-classical correlations between the sender and the receiver (Fig. 3d). Here, the entanglement success probability $p_{\mathrm{s,ent}} = 0.78 \pm 0.04$ is lower than for the state transfer, as success depends on both transmons remaining in the ground state (Supplementary Information). The fidelity of the joint state to the ideal Bell state is $\mathcal{F}_{\mathrm{Bell}} = 0.77 \pm 0.02$ (deterministic: $\mathcal{F}_{\mathrm{Bell,d}} \geq p_{\mathrm{s,ent}} \times \mathcal{F}_{\mathrm{Bell}} = 0.61 \pm 0.02$), confirming the successful generation of entanglement. We are able to achieve a net entanglement generation rate of $(140\,\mu\mathrm{s})^{-1}$ (for fidelity 0.77; equivalently $(110\,\mu\mathrm{s})^{-1}$ for fidelity 0.61, fully deterministic), limited by the average time it takes to reset the system ($\sim 100\,\mu\mathrm{s}$). This rate exceeds the single-photon loss in either memory ($<(450\,\mu\mathrm{s})^{-1}$), a strict requirement for scaling up the network size.

As the infidelity of our state transfer protocol is dominated by errors of a single type—photon loss—the scheme can be improved by selecting an appropriate error-correcting code. The use of cavity memories grants access to tools already developed for correcting loss in stationary states, such as redundantly encoding a qubit within a larger Hilbert space and using photon number parity as an error syndrome[29]. We choose a simple error-correctable code with minimal overhead, the $L=1$ binomial encoding, which has logical basis states $\{|0\rangle_L = |2\rangle, |1\rangle_L = (|0\rangle + |4\rangle)/\sqrt{2}\}$ (ref. [30]). Our transfer scheme is number-state independent, and so with no other modifications, we prepare and transmit the cardinal states of this encoding, again measuring the received state with Wigner tomography (Fig. 4a,b). These states have a larger average photon number ($\overline{n}=2$) relative to the single-photon encoding ($\overline{n}=0.5$), representing an additional 'overhead'. From this increased sensitivity to photon loss, we predict a mean fidelity of 0.60 and measure $\mathcal{F}_{\mathrm{avg}}=0.54\pm0.04$ in this manifold ($\mathcal{F}_{\mathrm{avg,d}}\geq0.47\pm0.04$) relative to the ideal states. Although its mean fidelity is lower than that of the single-photon encoding, the binomial encoding permits the use of parity as an error syndrome measurement.

This feature will enable detection and deterministic correction of single-photon loss errors. Above some transfer efficiency threshold, an error-corrected qubit would be transmitted with higher average fidelity than a qubit encoded in the single-photon manifold. Our efficiency ($\eta=0.74$) exceeds that of this 'break-even' threshold ($\eta\sim0.67$), defined as the crossing of simulated mean fidelities in each case (Fig. 3c). Beyond break-even, error correction can overcome the overhead associated with the binomial state encoding. Error correction is possible using high-fidelity quantum non-demolition parity measurements[29], which could be effectively realized by adding a dedicated readout channel to each module. Following this measurement, fast feedback could be used to apply a conditional correction pulse. Along with modest improvements to the release and capture efficiencies, error correction should place the transfer firmly within this advantageous regime. Optimization over a wider set of bosonic codes could produce even larger improvement (Supplementary Information). These error correction concepts can also be extended to improve entanglement fidelity without sacrificing the determinism of the protocol.

In summary, we have realized a high-fidelity, deterministic quantum state transfer protocol between remote microwave cavity memories using tools available in superconducting cavity circuit quantum electrodynamics. This protocol can also be performed between other systems, such as transmon qubits[31,32]. Importantly, our implementation is capable of transferring both single- and multiphoton quantum states. This allows use of a multiphoton qubit encoding that, while initially producing larger overhead and reducing mean fidelity, extends the techniques of quantum error correction to enable the mitigation of photon loss in transmission. The demonstration of remote entanglement generation at a rate exceeding the memory loss rates satisfies an essential requirement for scalable quantum communication and distributed computation[33]. Entanglement is a critical resource in quantum networks, and its rapid and on-demand generation will enable high-level operations between remote modules such as non-local gates[34] and entanglement distillation[35,36]. Our experimental results thus demonstrate precise and tunable coupling of modular superconducting circuit systems that can be used to develop large-scale fault-tolerant quantum computing and communication networks.

Methods

Methods, including statements of data availability and any associated accession codes and references, are available at https://doi.org/10.1038/s41567-018-0115-y.

Received: 23 December 2017; Accepted: 14 March 2018;
Published online: 23 April 2018

References

1. Kimble, H. J. The quantum internet. *Nature* **453**, 1023–1030 (2008).
2. Northup, T. E. & Blatt, R. Quantum information transfer using photons. *Nat. Photon.* **8**, 356–363 (2014).
3. Jiang, L., Taylor, J. M., Sørensen, A. S. & Lukin, M. D. Distributed quantum computation based on small quantum registers. *Phys. Rev. A.* **76**, 062323 (2007).
4. Nickerson, N. H., Li, Y. & Benjamin, S. C. Topological quantum computing with a very noisy network and local error rates approaching one percent. *Nat. Commun.* **4**, 1756 (2013).
5. Monroe, C. et al. Large-scale modular quantum-computer architecture with atomic memory and photonic interconnects. *Phys. Rev. A.* **89**, 022317 (2014).
6. Chou, C. W. et al. Measurement-induced entanglement for excitation stored in remote atomic ensembles. *Nature* **438**, 828–832 (2005).
7. Moehring, D. L. et al. Entanglement of single-atom quantum bits at a distance. *Nature* **449**, 68–71 (2007).
8. Ritter, S. et al. An elementary quantum network of single atoms in optical cavities. *Nature* **484**, 195–200 (2012).
9. Hofmann, J. et al. Heralded entanglement between widely separated atoms. *Science* **337**, 72–75 (2012).
10. Bernien, H. et al. Heralded entanglement between solid-state qubits separated by three metres. *Nature* **497**, 86–90 (2013).
11. Roch, N. et al. Observation of measurement-induced entanglement and quantum trajectories of remote superconducting qubits. *Phys. Rev. Lett.* **112**, 170501 (2014).
12. Narla, A. et al. Robust concurrent remote entanglement between two superconducting qubits. *Phys. Rev. X* **6**, 031036 (2016).
13. Olmschenk, S. et al. Quantum teleportation between distant matter qubits. *Science* **323**, 486–489 (2009).
14. Stute, A. et al. Quantum-state transfer from an ion to a photon. *Nat. Photon.* **7**, 219–222 (2013).
15. Pfaff, W. et al. Unconditional quantum teleportation between distant solid-state quantum bits. *Science* **345**, 532–535 (2014).
16. Cirac, J. I., Zoller, P., Kimble, H. J. & Mabuchi, H. Quantum state transfer and entanglement distribution among distant nodes in a quantum network. *Phys. Rev. Lett.* **78**, 3221–3224 (1997).
17. Pechal, M. et al. Microwave-controlled generation of shaped single photons in circuit quantum electrodynamics. *Phys. Rev. X* **4**, 041010 (2014).
18. Yin, Y. et al. Catch and release of microwave photon states. *Phys. Rev. Lett.* **110**, 107001 (2013).
19. Srinivasan, S. J. et al. Time-reversal symmetrization of spontaneous emission for quantum state transfer. *Phys. Rev. A.* **89**, 033857 (2014).
20. Pfaff, W. et al. Controlled release of multiphoton quantum states from a microwave cavity memory. *Nat. Phys.* **13**, 882–887 (2017).
21. Wenner, J. et al. Catching time-reversed microwave coherent state photons with 99.4% absorption efficiency. *Phys. Rev. Lett.* **112**, 210501 (2014).
22. Flurin, E., Roch, N., Pillet, J. D., Mallet, F. & Huard, B. Superconducting quantum node for entanglement and storage of microwave radiation. *Phys. Rev. Lett.* **114**, 090503 (2015).
23. Reed, A. P. et al. Faithful conversion of propagating quantum information to mechanical motion. *Nat. Phys.* **13**, 1163–1167 (2017).
24. Axline, C. et al. An architecture for integrating planar and 3D cQED devices. *Appl. Phys. Lett.* **109**, 042601 (2016).
25. Schuster, D. I. et al. Resolving photon number states in a superconducting circuit. *Nature* **445**, 515–518 (2007).
26. Bishop, L. S., Ginossar, E. & Girvin, S. M. Response of the strongly driven Jaynes–Cummings oscillator. *Phys. Rev. Lett.* **105**, 100505 (2010).
27. Sank, D. et al. Measurement-induced state transitions in a superconducting qubit: beyond the rotating wave approximation. *Phys. Rev. Lett.* **117**, 190503 (2016).
28. Massar, S. & Popescu, S. Optimal extraction of information from finite quantum ensembles. *Phys. Rev. Lett.* **74**, 1259–1263 (1995).
29. Ofek, N. et al. Extending the lifetime of a quantum bit with error correction in superconducting circuits. *Nature* **536**, 441–445 (2016).
30. Michael, M. H. et al. New class of quantum error-correcting codes for a bosonic mode. *Phys. Rev. X* **6**, 031006 (2016).
31. Campagne-Ibarcq, P. et al. Deterministic remote entanglement of superconducting circuits through microwave two-photon transitions. Preprint at http://arxiv.org/abs/1712.05854 (2017).
32. Kurpiers, P. et al. Deterministic quantum state transfer and generation of remote entanglement using microwave photons. Preprint at http://arxiv.org/abs/1712.08593 (2017).
33. Hucul, D. et al. Modular entanglement of atomic qubits using photons and phonons. *Nat. Phys.* **11**, 37–42 (2015).
34. Gottesman, D. & Chuang, I. L. Demonstrating the viability of universal quantum computation using teleportation and single-qubit operations. *Nature* **402**, 390–393 (1999).

35. Bennett, C. H. et al. Purification of noisy entanglement and faithful teleportation via noisy channels. *Phys. Rev. Lett.* **76**, 722–725 (1996).
36. Deutsch, D. et al. Quantum privacy amplification and the security of quantum cryptography over noisy channels. *Phys. Rev. Lett.* **77**, 2818–2821 (1996).

Acknowledgements

The authors would like to acknowledge valuable discussions with C. Zhou, A. Narla, S. Shankar and K.W. Lehnert. This work was supported by the US Army Research Office (W911NF-14-1-0011). C.J.A. was supported by the NSF Graduate Research Fellowship (DGE-1122492); L.D.B. by the ARO QuaCGR Fellowship; W.P. by the NSF (PHY1309996) and by a fellowship instituted with a Max Planck Research Award from the Alexander von Humboldt Foundation; W.P., P.R. and M.Z. by the US Air Force Office of Scientific Research (FA9550-15-1-0015); S.M.G by the NSF (DMR-1609326); L.J. by the Alfred P. Sloan Foundation (BR2013-049) and the Packard Foundation (2013-39273). Facilities use was supported by the Yale Institute for Nanoscience and Quantum Engineering (YINQE) and the Yale SEAS cleanroom.

Author contributions

C.J.A., L.D.B. and W.P. performed the experiment and analysed the data under the supervision of R.J.S. C.J.A. and L.F. fabricated the transmon qubits. M.Z. assisted in data analysis and ran supporting simulations. M.Z., S.M.G. and L.J. provided theory support. K.C. assisted in development of a Wigner reconstruction algorithm. P.C.-I. contributed to the experimental design under the supervision of M.H.D. P.R. developed optimal control pulse software and implemented field measurement capability. C.J.A., L.D.B., W.P. and R.J.S. wrote the manuscript with contributions from all authors.

Competing interests

R.J.S., M.H.D. and L.F. are founders, and R.J.S. and L.F. are equity shareholders of Quantum Circuits, Inc.

Additional information

Supplementary information is available for this paper at https://doi.org/10.1038/s41567-018-0115-y.

Reprints and permissions information is available at www.nature.com/reprints.

Correspondence and requests for materials should be addressed to C.J.A. or L.D.B. or W.P. or R.J.S.

Publisher's note: Springer Nature remains neutral with regard to jurisdictional claims in published maps and institutional affiliations.

Methods

Samples and set-up. Devices are assembled using a shared-chip transmon qubit and stripline readout resonator, inserted into a high-Q three-dimensional coaxial stub cavity. The system is cooled to $T \approx 20$ mK in a dilution refrigerator. Signals are introduced and IQ-modulated using microwave generators as local oscillators and a field-programmable gate array (FPGA) system with integrated analog-to-digital converter and digital-to-analog converter, and remain phase-locked. Output signals are amplified with a Josephson parametric converter, high-electron-mobility transistor (HEMT) amplifier and room-temperature amplifiers, permitting single-shot readout with fidelity ≥0.93. Communication frequencies are tuned to match by adjusting a mechanical micropositioning stage, which drives a superconducting pin near the stripline resonator to adjust the capacitance, and thus the frequency. The system is initialized before each measurement by an active-feedback cooling sequence. State manipulation pulses aside from qubit rotations and cavity displacements are generated using optimal control techniques.

Measurements. Cavity spectroscopy is performed by selectively mapping cavity excitation number ($\overline{n}$) onto the qubit state, and is used to calculate efficiency values. Wigner tomography is performed by a displaced parity measurement, and is reconstructed using a maximum-likelihood estimation algorithm to calculate state fidelities. Both measurement types are normalized and constrained to be physical to produce the 'conditioned' data presented.

Wavepacket shaping. The temporal shape of the pulses modulating the conversion process pump are calculated numerically. Accounting for dynamic Stark shifts and imposing the prescribed shape of the travelling wavepacket, we solve the set of differential equations of motion between the memory and communication modes in each module. We thus obtain the coupling $g^{s,r}(t)$ and convert this into a pump strength using independent calibration of the pumps' Stark shifts by transmon spectroscopy.

To allow the propagating wavepacket to be absorbed by a receiving cavity, both the sender and receiver systems must expect the same temporal wavepacket shape. To separate the problem into two parts, we first specify the shape of this wavepacket, $b_{\mathrm{out}}(t)$, and then calculate the pump amplitudes needed at the sender and the receiver to match the coupling rate $g_j(t)$ to this wavepacket, where the system subscript $j = s$ (r) denotes the sender (receiver). When correctly calculated, energy will transfer between the sender, the propagating mode, and the receiver at matching rates. Here we detail the calculation of the drive amplitudes that make this possible. Since we treat the two systems individually, the system subscript j will be omitted for clarity wherever possible.

Shaping the released wavepacket. In the rotating frame of the pumps, the Hamiltonian enabling conversion between memory and output modes a and b is

$$H_{\mathrm{conv}}(t) = i\left(g(t)\hat{a}\hat{b}^{\dagger} - g^{*}(t)\hat{a}^{\dagger}\hat{b}\right) \tag{1}$$

with

$$g(t) = g\left(\xi_1(t), \xi_2\right) \tag{2}$$

The correspondence producing the conversion rate $g(t)$ as a function of the two applied pump amplitudes ξ_1 and ξ_2 is calibrated experimentally (Supplementary Information). In the lowest-order approximation, $g_j \propto \xi_1^{j}\xi_2^{j}$.

As the conversion always depends on both pumps, only one of the two pumps needs to vary in time to produce any particular $g(t)$. For experimental convenience, we designate ξ_1 to vary in time. The pump ξ_2 is held constant in time, with a smooth (~200 ns) ring-up and ring-down profile.

One significant effect of the application of pumps is ac-Stark shifts that shift the frequency of the modes. The Stark shifts during the transfer process are a function of both pump amplitudes:

$$H_{\mathrm{Stark}}(t) = \delta_{\mathrm{a}}(t)\hat{a}^{\dagger}\hat{a} + \delta_{\mathrm{b}}(t)\hat{b}^{\dagger}\hat{b} \tag{3}$$

Each Stark shift depends on each pump amplitude:

$$\delta_{\mathrm{a}}(t) = \delta_{\mathrm{a}}\left(\xi_1(t), \xi_2\right) \quad \delta_{\mathrm{b}}(t) = \delta_{\mathrm{b}}\left(\xi_1(t), \xi_2\right) \tag{4}$$

This shift is calibrated independently (Supplementary Information). We find very good agreement with the expected dependence, which is linear in the sum of the pump powers:

$$\begin{aligned} \delta_{\mathrm{a}}(t) &= 2\chi_{\mathrm{aa}}\,|\xi_1(t)|^2 + \chi_{\mathrm{ab}}\,|\xi_2|^2 \\ \delta_{\mathrm{b}}(t) &= 2\chi_{\mathrm{bb}}\,|\xi_2(t)|^2 + \chi_{\mathrm{ab}}\,|\xi_1|^2 \end{aligned} \tag{5}$$

Having established the dependence of both the conversion rate $g(t)$ and the Stark shifts δ_{a}, δ_{b}, we can write down the equations of motion for the modes $\hat{a}$ and $\hat{b}$ of the sender:

$$\dot{a}(t) = -g(\xi_1(t), \xi_2)b(t) - i\delta_{\mathrm{a}}(\xi_1(t), \xi_2)a(t) \tag{6a}$$

$$\dot{b}(t) = g^{*}(\xi_1(t), \xi_2)a(t) - i\delta_{\mathrm{b}}(\xi_1(t), \xi_2)b(t) - \frac{\kappa_{\mathrm{out}}}{2}b(t) \tag{6b}$$

$$b(t) = b_{\mathrm{out}}(t)/\sqrt{\kappa_{\mathrm{out}}} \tag{6c}$$

As these equations are linear, we can consider the evolution of the expectation values of the field operators $\hat{a}$ and $\hat{b}$, so we have dropped the operator notation. This will also allow us to solve the problem classically, which is computationally simpler compared to a full quantum simulation.

Equation (6c) is the input–output relation, taking as an assumption that there is no incoming field. In this case, for a chosen $b_{\mathrm{out}}(t)$ and ξ_2, the only undetermined quantities are $a(t)$ and $\xi_1(t)$. In what follows, we suppress the time dependence and the explicit dependence on the static ξ_2 for simplicity.

The goal is to eliminate a, leaving an equation for g in terms of b that can be solved numerically. We first note that equation (6b) can be written as

$$g^{*}(\xi_1)a = \dot{b} + i\delta_{\mathrm{b}}(\xi_1)b + \frac{\kappa_{\mathrm{out}}}{2}b \tag{7}$$

with the derivative

$$\dot{g}^{*}(\xi_1)a + g^{*}(\xi_1)\dot{a} = \ddot{b} + i\dot{\delta}_{b}(\xi_1)b + i\delta_{\mathrm{b}}(\xi_1)\dot{b} + \frac{\kappa_{\mathrm{out}}}{2}\dot{b} \tag{8}$$

We can multiply equation (6a) by $g^{*}(\xi_1)$ and substitute it into equation (8) to write

$$\dot{g}^{*}(\xi_1)a - |g(\xi_1)|^2 b - i\delta_{\mathrm{a}}(\xi_1)g^{*}(\xi_1)a = \ddot{b} + i\dot{\delta}_{b}(\xi_1)b + i\delta_{\mathrm{b}}(\xi_1)\dot{b} + \frac{\kappa_{\mathrm{out}}}{2}\dot{b} \tag{9}$$

Finally, multiplying equation (9) by $g^{*}(\xi_1)$, which is given by equation (7), yields

$$\begin{aligned} &\left[\dot{g}^{*}(\xi_1) - i\delta_{\mathrm{a}}(\xi_1)g^{*}(\xi_1)\right]\left[\dot{b} + i\delta_{\mathrm{b}}(\xi_1)b + \frac{\kappa_{\mathrm{out}}}{2}b\right] - g^{*}(\xi_1)\,|g(\xi_1)|^2\, b \\ &= g^{*}(\xi_1)\ddot{b} + i\dot{\delta}_{b}(\xi_1)g^{*}(\xi_1)b + i\delta_{\mathrm{b}}(\xi_1)g^{*}(\xi_1)\dot{b} + \frac{\kappa_{\mathrm{out}}}{2}g^{*}(\xi_1)\dot{b} \end{aligned} \tag{10}$$

Equation (10) is solved numerically to give the correct $\xi_1(t)$ for a given $b_{\mathrm{out}}(t)$. The initial condition $\xi_1(t=0)$ comes from equation (7). This process inherently accounts for the Stark shifts in two ways. First, $\xi_1(t)$ will have a phase that varies in time. This dynamic frequency control ensures that $b_{\mathrm{out}}(t)$ can have a fixed frequency, even when the mode a does not. Second, the amplitude of $\xi_1(t)$ will change in time in a way that accounts for the frequency shift of the output mode b: the amplitude will increase to compensate for the fact that the conversion process is effectively off-resonant. By scaling the output field $b_{\mathrm{out}}(t)$ to specify the amount of energy contained therein, we calculate different pump waveforms for full and partial release via the same procedure. While the equations of motion are linear in a and b, equation (10) is clearly nonlinear in ξ_1. This is why the pulses for full and partial releases are not simply scaled versions of one another, even though the released wavepackets $b_{\mathrm{out}}(t)$ are. For this reason, the capture pulse will remain unchanged and independent of the release pulse.

Wavepacket capture. The calculation of the pump waveform required to capture the propagating wavepacket is very similar to the above. The equations of motion for the receiver are

$$\dot{a}(t) = -g(\xi_1(t), \xi_2)b(t) - i\delta_{\mathrm{a}}(\xi_1(t), \xi_2)a(t) \tag{11a}$$

$$\dot{b}(t) = g^{*}(\xi_1(t), \xi_2)a(t) - i\delta_{\mathrm{b}}(\xi_1(t), \xi_2)b(t) - \frac{\kappa_{\mathrm{out}}^{r}}{2}b(t) + \sqrt{\kappa_{\mathrm{out}}^{r}}\,b_{\mathrm{in}}^{r}(t) \tag{11b}$$

$$b(t) = b_{\mathrm{out}}^{r}(t)/\sqrt{\kappa_{\mathrm{out}}^{r}} + b_{\mathrm{in}}^{r}(t)/\sqrt{\kappa_{\mathrm{out}}^{r}} \tag{11c}$$

which are identical to equations (6a), (6b) and (6c), with the difference that there now exists an input field term $b_{\mathrm{in}}^{r}(t)$. For clarity, we now restore the superscripts s and r for the sender and the receiver, respectively. To calculate the capture waveform, we specify that this input field has the shape of the released wavepacket: $b_{\mathrm{in}}^{r}(t) = b_{\mathrm{out}}^{s}(t)$, and that the field reflected off the receiver is zero: $b_{\mathrm{out}}^{r}(t) = 0$, which corresponds to perfect absorption. Taken together, these constraints imply

$$\dot{a}(t) = -g(\xi_1(t), \xi_2)b(t) - i\delta_{\mathrm{a}}(\xi_1(t), \xi_2)a(t) \tag{12a}$$

$$\dot{b}(t) = g^{*}(\xi_1(t), \xi_2)a(t) - i\delta_b(\xi_1(t), \xi_2)b(t) + \frac{\kappa^{r}_{out}}{2}b(t) \quad (12b)$$

$$b(t) = b^{s}_{out}(t)/\sqrt{\kappa^{r}_{out}} \quad (12c)$$

which look just like equations (6a), (6b) and (6c), but with the sign of κ_{out} changed. The procedure for obtaining $\xi_1(t)$ is the same as for the sender. The only major difference is that this equation is solved in reverse, with the final condition specifying the occupation of a at the end of the protocol. This corresponds to the fraction of incoming energy that is absorbed, $\eta^{(r)}_{trunc}$ (Supplementary Information). Increasing this fraction corresponds to increasing the pump strength beyond what is achievable in our system.

Importantly, the capture waveform is the same for both full and partial release; this is due to the linearity of the equations of motion (equations (11a), (11b) and (11c)) on $b^{r}_{in}(t)$; in other words, the capture is state-independent. Therefore, the capture waveform depends only on the shape of the incoming wavepacket, not its amplitude.

Choice of wavepacket shape. The envelope of the wavepacket $|b_{out}(t)|$ is an arbitrary choice, up to constraints on the bandwidth of the conversion process. For experimental convenience, we choose $|b_{out}(t)| \propto 1-\cos^2\left(\frac{\pi t}{T}\right)$, where $T = 6\,\mu s$ is the total transfer time. We find empirically that this smooth shape reduces the maximum pump amplitudes required for a given transfer time as compared to other shapes tested. The frequency of the wavepacket is also free to be varied. We choose a frequency ~ 1 MHz below the static frequencies of the communication modes, to account for Stark shifts (which are always negative) while the pumps are applied.

Supplementary methods. For more details including those regarding operations, analysis and determination of uncertainties, see the Supplementary Information. 'Unconditioned' and supplementary data are also presented.

Data availability. The data that support the plots within this paper and other findings of this study are available from the corresponding author upon reasonable request.